Increasing river alkalinity slows ocean acidification in the northern Gulf of Mexico

Fabian A Gomez[1], Rik Wanninkhof[2], Leticia Barbero[3], and Sang-Ki Lee[4]

[1]Mississippi State University
[2]OCD/AOML/NOAA
[3]National Oceanic and Atmospheric Administration (NOAA)
[4]Atlantic Oceanographic and Meteorological Laboratory (NOAA)

November 21, 2022

Abstract

Ocean acidification (OA) progression is affected by multiple factors, such as ocean warming, biological production, and runoff. Here we used an ocean-biogeochemical model to assess the impact of river runoff and climate variability on the spatiotemporal patterns of OA in the Gulf of Mexico (GoM) during 1981-2014. The model showed the expected pH and aragonite saturation state (ΩAr) decline, due to the increase in anthropogenic carbon, with trends close to values reported for the Subtropical North Atlantic. However, significant departures from the basin-averaged pattern were obtained in part of the northern GoM shelf, where pH and ΩAr increased. Model sensitivity analyses showed that OA progression was counteracted by enhanced alkalinity from the Mississippi-Atchafalaya River System. Our findings highlight that river alkalinity is a key driver of carbon system variability in river-dominated ocean margins and emphasize the need to quantify riverine chemistry to properly assess acidification in coastal waters.

Increasing river alkalinity slows ocean acidification in the northern Gulf of Mexico

Fabian A. Gomez[1,2], Rik Wanninkhof[2], Leticia Barbero[3,2], Sang-Ki Lee[2]

[1]Northern Gulf Institute, Mississippi State University, Starkville, Mississippi, USA.

[2]NOAA Atlantic Oceanographic and Meteorological Laboratory, Miami, Florida, USA.

[3]Cooperative Institute for Marine and Atmospheric Studies, University of Miami, Miami, Florida, USA.

Corresponding author: Fabian A. Gomez (fabian.gomez@noaa.gov)

Key Points:

- We simulated the spatiotemporal variability of ocean acidification progression over the Gulf of Mexico during 1981-2014.
- Model results showed positive trends in the surface ocean alkalinity, salinity, and temperature influencing acidification trends.
- Increasing Mississippi river alkalinity substantially lessened the ocean acidification progression on the northern Gulf of Mexico shelf.

Abstract

Ocean acidification (OA) progression is affected by multiple factors, such as ocean warming, biological production, and runoff. Here we used an ocean-biogeochemical model to assess the impact of river runoff and climate variability on the spatiotemporal patterns of OA in the Gulf of Mexico (GoM) during 1981-2014. The model showed the expected pH and aragonite saturation state (Ω_{Ar}) decline, due to the increase in anthropogenic carbon, with trends close to values reported for the Subtropical North Atlantic. However, significant departures from the basin-averaged pattern were obtained in part of the northern GoM shelf, where pH and Ω_{Ar} increased. Model sensitivity analyses showed that OA progression was counteracted by enhanced alkalinity from the Mississippi-Atchafalaya River System. Our findings highlight that river alkalinity is a key driver of carbon system variability in river-dominated ocean margins and emphasize the need to quantify riverine chemistry to properly assess acidification in coastal waters.

Plain Language Summary

Although ocean acidification (OA) is mainly driven by the ocean uptake of anthropogenic carbon dioxide from the atmosphere, multiple factors influence its temporal progression, including changes in ocean temperature, biological processes, and river discharge. Here we used numerical model outputs to describe historical OA trends across the Gulf of Mexico (GoM) and identify the main drivers of its spatial variability. We showed that changes in river runoff slowed OA over the northern GoM coast. This was mainly due to an increasing Mississippi river alkalinity concentration, a property related to the water capacity to neutralize acidification. Our results show the importance of alkalinity changes to quantify OA progression in the GoM.

1 Introduction

Ocean acidification (OA), induced by the ocean uptake of atmospheric anthropogenic CO_2, is affecting global ocean carbon chemistry, leading to a sustained decline in pH, along with an increase in dissolved inorganic carbon (DIC), partial pressure of CO_2 (pCO_2), and calcium carbonate solubility, the latter usually tracked as a decline in aragonite saturation state (Ω_{Ar}) (Doney et al., 2009; Gruber et al., 2019). These changes in carbon chemistry are negatively impacting marine species and ecosystems. The most obvious impacts are associated with decreased calcification rates in calcifying organisms, such as corals and shellfish, which results in reduced individual growth and survival (e.g., Hoegh-Guldberg et al., 2007; Waldbusser et al., 2015). OA

is a major environmental stressor, which is expected to produce significant changes in marine community structure and the availability of marine resources (Ekstrom et al., 2015; Cross et al., 2019; Doney et al., 2020).

Datasets with records extending two or more decades have revealed long-term pCO_2 increases consistent with the increase in atmospheric CO_2, but variability is evident across regions (Bates et al., 2014; Lauvset et al., 2015). Major departures from the anthropogenic CO_2-driven changes can be expected in coastal regions, where variability in biological production, coastal currents, temperature, and salinity are more likely to impact carbon chemistry trends (Cai et al., 2011; Turi et al., 2016; Laruelle et al., 2018; Salisbury & Jönsson, 2018). This is particularly true in river dominated ocean margins where the chemistry of river discharge directly influences the ability of coastal waters to counteract acidification (Duarte et al., 2013,). Therefore, sustained observational programs and modeling are required to identify OA progression and causes at regional levels, so that ecosystem and socioeconomic vulnerabilities to OA can be assessed.

The Gulf of Mexico (GoM) hosts large spatiotemporal variability in its physical and biogeochemical patterns and is significantly influenced by the Loop Current and the Mississippi-Atchafalaya River System (MARS). The Loop Current transports warm and oligotrophic waters from the Caribbean Sea, and largely defines water properties in the open GoM (Muller-Karger et al., 2015; Damien et al., 2018). The MARS delivers large freshwater and nutrients fluxes to the northern GoM shelf, strongly modulating regional salinity and biochemistry patterns (Dagg & Breed, 2003; Rabalais et al., 2007). A series of observational studies have documented the dominant spatial patterns and seasonal variability of pCO_2 and other carbon system variables in the GoM (e.g., Lohrenz et al., 2018; Wang et al., 2013; Wanninkhof et al., 2015; Hu et al., 2015, 2018). However, interannual to multi-decadal variability remains poorly examined due to the lack of sufficiently long time-series capable of discriminating OA trends from natural variability.

High-resolution ocean-biogeochemical models can assist in filling observational gaps by describing and attributing ocean chemistry variability over time. Therefore, they are particularly valuable tools for assessing the historical progression of OA and other low-frequency processes that impact the carbon cycle. In a recent study, Gomez et al. (2020) configured and validated an ocean-biogeochemical model for the GoM, examining dominant seasonal patterns in pCO_2 and Ω_{Ar}. For the present study, we used the same model to investigate OA progression. We derived

long-term trends for OA indicators during 1981-2014 and performed sensitivity analyses to examine the influence of river runoff and climate variability on OA progression.

2 Methods

We used the ocean-biogeochemical model described and validated in Gomez et al. (2018, 2020), which contains 16 state variables, including two inorganic carbon system variables: total alkalinity (TA) and DIC. The ocean-biogeochemical model was implemented in the Regional Ocean Model System (ROMS, Shchepetkin et al., 2005), with a horizontal resolution of ~8 km and 37 sigma-coordinate vertical levels. A third order upstream scheme and a fourth order Akima scheme were used for horizontal and vertical momentum, respectively. A multidimensional positive definite advection transport algorithm (MPDATA) was used for tracer advection, while a Mellor and Yamada 2.5-level closure scheme was used to resolve vertical turbulence. The initial and open boundary conditions were derived from a 25 km horizontal resolution model for the North Atlantic (Liu et al., 2015). Surface fluxes of momentum (6-hour resolution), heat (daily), and precipitation (monthly) were derived from the European Centre for Medium Range Weather Forecasts reanalysis product ERA-Interim (Dee et al., 2011) using a bulk flux parameterization. River discharge, nutrients, TA, and DIC data were obtained from the U.S. Geological Survey for rivers in the U.S. and derived from scientific literature for Mexican rivers (He et al. 2011; Muñoz-Salinas & Castillo, 2015; Martínez-López & Zavala-Hidalgo, 2009). We prescribed a time-evolving monthly series of freshwater discharge for 28 river sources in the U.S., and a climatological discharge for 10 rivers in the U.S. and 11 rivers in Mexico. Due to the lack of continuous long-term records, the time evolving concentration of nutrients, TA, and DIC were prescribed for only the Mississippi and Atchafalaya rivers, while long-term climatological values were prescribed for the other river sources. The partial pressure of atmospheric CO_2 (pCO_{2air}) was prescribed as a continuous nonlinear function (using a third-degree polynomial expression plus four harmonics) adjusted to the monthly pCO_{2air} series from the Mauna Loa Observatory.

In addition to the model hindcast, we also conduct two experiments to evaluate the OA progression sensitivity to river runoff changes: the climatological MARS chemistry experiment (CLM_MC) and the climatological rivers experiment (CLM_RIV). In CLM_MC, we used monthly climatological values for the MARS's chemistry (nutrients, DIC, and TA). In CLM_RIV,

we used climatological river discharge values for all rivers, as well as the climatological chemistry for the MARS. The influence of MARS's time evolving chemistry on OA was obtained from the difference between the CLM_MC and hindcast trends, and the added impact of time evolving river discharges and time-evolving MARS chemistry from the difference between the CLM_RIV and hindcast trends. Hence, the difference between the CLM_MC and CLM_RIV trends provided an estimate of the discharge variability impacts on OA. Finally, to evaluate the influence of climate variability on the OA patterns, we conducted the climatological forcing experiment (CLM_FORC), where we prescribed climatological patterns for rivers, surface fluxes and the open boundary conditions at the southern and eastern edges of the model domain. The only exceptions were pCO_{2air} and the open boundary conditions for DIC, which varied as in the model hindcast (following Turi et al., 2016). The climate-variability impact was derived from the difference between the CLM_FORC and hindcast trends.

Monthly outputs of surface DIC (*s*DIC), surface TA (*s*TA), sea surface salinity (SSS), and sea surface temperature (SST) were used to derive simulated in situ patterns of three OA indicators: pCO_2, pH, and Ω_{Ar}. To this effect, we used the CO2SYS program for CO_2 System Calculations (van Heuven et al., 2011). A simple linear regression was used to calculate the trends from the model's monthly anomalies for each variable of interest. Monthly outputs with the monthly climatological mean of 1981-2014 removed (deseasonalized) were referred to as anomalies.

We used a first order Taylor series to decompose the surface pCO_2, pH, and Ω_{Ar} variability into their four driver's components:

$$\Delta\varphi \approx \frac{\partial\varphi}{\partial sDIC} \cdot \Delta sDIC + \frac{\partial\varphi}{\partial sTA} \cdot \Delta sTA + \frac{\partial\varphi}{\partial SSS} \cdot \Delta SSS + \frac{\partial\varphi}{\partial SST} \cdot \Delta SST \qquad \textbf{(1)}$$

where $\Delta\varphi$ represents the time change for the parameter of interest (either pCO_2, pH, or Ω_{Ar}), and the four right side terms represent the *s*DIC, *s*TA, SSS, and SST contribution to the φ change, respectively. The partial derivatives of the contribution terms were estimated by adding a small perturbation to each driver while keeping the other three terms as constant, using the CO2SYS program for the carbon system calculations.

3 Results

The simulated patterns of surface pCO_2, pH, and Ω_{Ar} anomalies produced basin-averaged trends of 1.57 ± 0.03 μatm yr^{-1}, –0.0015 ± 0.0000 yr^{-1}, and –0.0087 ± 0.0002 yr^{-1} during 1981-2014, respectively. The mean surface pCO_2 trend was somewhat smaller than the growth of atmospheric CO_2, which was at a mean rate of 1.68 μatm yr^{-1} over the same period. Large spatial variability was evident in the modeled trends (Figures 1a–1c; Table S1), suggesting that local processes were influencing the long-term changes. The largest departures from the basin-averaged values were located near the MARS delta, in the central part of the northern GoM shelf, where negative pCO_2 trends and positive Ω_{Ar} and pH trends were obtained nearshore. As a result, the average trend on the northern GoM inner shelf (bottom depth < 25 m; Figure 1f) was 0.93 ± 0.10 μatm yr^{-1}, –0.0009 ± 0.0001 yr^{-1} and –0.0003 ± 0.0009 yr^{-1} for pCO_2, pH and Ω_{Ar}, respectively, the slowest rates compared to those in other shelves and the open GoM. The modeled long-term changes in surface pCO_2 impacted the air-sea CO_2 flux (Figure 1d, Table S1). The most prominent feature was on the northern GoM inner shelf, where the CO_2 flux trend was strongly negative (increase in carbon uptake), averaging –0.018 ± 0.003 mol m^{-2} yr^{-2} for a mean flux of –0.844 mol m^{-2} yr^{-1}, but reaching maximum trend magnitude rates greater than –0.050 mol m^{-2} yr^{-2} near the MARS delta. The basin-averaged flux trend was –0.004 ± 0.001 mol m^{-2} yr^{-2} for a model mean flux of –0.382 mol m^2 yr^{-1}.

Changes in surface pCO_2, pH, and Ω_{Ar} are connected to changes in DIC, TA, salinity, and temperature. Both pH and Ω_{Ar} increase with TA and decrease with DIC and salinity. However, their response to temperature differs, as warming decreases calcium carbonate solubility (increasing Ω_{Ar}) but promotes hydrogen ion formation (decreasing pH). pCO_2 displays the opposite pattern to that of pH, increasing with DIC, salinity, and temperature, and decreasing with TA. A potential reason for the small pCO_2, pH, and Ω_{Ar} trends on the northern GoM shelf could be an increased biological uptake of DIC that counteracts the DIC increase due to anthropogenic CO_2. However, the simulated surface net community production –the difference between phytoplankton production and community respiration– displayed a weak negative trend near the MARS delta, linked to decreased river discharge and nutrient runoff (Figure 1e). Consequently, a biologically driven offset of the modeled OA trends was discarded.

To identify processes responsible for the simulated OA pattern, we examined the Taylor decomposition of the pCO_2, pH, and Ω_{Ar} trends. The patterns showed that sDIC, which had a basin-

averaged growth of 1.16 ± 0.02 μmol kg^{-1} yr^{-1}, dominated the total trend variability (Figures 2a–2c; Figure 3a; Table S1). The greatest sDIC impact was on the northern GoM inner shelf, where the sDIC trend was 1.7 times the basin value. This implied that the slow OA progression in the region was not driven by sDIC. Instead, the main process responsible for the slow acidification was a significant sTA growth of 1.90 ± 0.22 μmol kg^{-1} yr^{-1}, which largely counteracted the sDIC-induced changes (Figures 2d–2f; Figure 3b; Table S1). The contributions of SSS and SST to the pCO_2, pH, and Ω_{Ar} trends were relatively minor (Figures 2g–2l). The salinity increase, which averaged 0.007 yr^{-1} over the GoM basin and reached values greater than 0.020 yr^{-1} over the northern GoM shelf and the southern part of the West Florida shelf (Figure 3c; Table S1), strengthened the OA pattern. Surface warming, which was 0.008 ± 0.002 °C yr^{-1} on average across the GoM basin (Figure 3d; Table S1), contributed to increase the magnitude of the pH and pCO_2 trends, and had a weak positive impact on Ω_{Ar}. Although small in magnitude, the SSS and SST-induced changes influenced the spatial OA pattern. If we removed the SSS and SST contribution from the total trends, a smoother trend pattern was obtained (Figure S1).

The trend decomposition revealed that sTA played a key role as driver of the simulated OA trends around the MARS delta. Strong sTA growth on the northern GoM shelf, as well as the enhanced sDIC trend, could be linked to changes in MARS chemistry. This was evident when we compared the low-frequency TA and DIC changes for the MARS and the surface northern GoM shelf waters (Figure S2). The TA and DIC from the MARS increased about 5 and 3 μmol kg^{-1} yr^{-1} during 1981-2014, respectively (Table S2). Declining trends in river discharge (–67 ± 54 m^3 s^{-1} yr^{-1} for the MARS; –53 ± 19 m^3 s^{-1} yr^{-1} for rivers other than MARS) could also contribute to the nearshore sTA and sDIC increase. This is because most rivers along the northern GoM coast, excluding those in the southern and central Texas coast, have relatively low TA and DIC concentration compared to the ocean values; thus, a decreasing discharge implies a reduced influence of the river's dilution effect on these two variables. To quantify the influence of rivers on the ocean carbonate system, we examined the patterns derived from the CLM_RIV and CLM_MC experiments and compared them with the model hindcast. Over the northern GoM shelf, CLM_RIV showed that changes in river discharge and MARS chemistry accounted for 84% of the hindcast sTA trend and 40% of the hindcast sDIC trend (Figures 3e and 3f; Table S3). Over the same region, CLM_MC showed that the MARS chemistry changes (excluding river flow changes) accounted for 61% of the hindcast sTA trend and 32% of the hindcast sDIC trend (Figures S3a and

S3b; Table S3). Consequently, changes in river discharge (CLM_MC minus CLM_RIV) accounted for 23% and 8% of the hindcast's TA and DIC trends, respectively (Figures S3e and S3f). Although the sTA trend substantially decreased in the CLM_RIV experiment, a residual TA trend remained across the basin, consistent with a positive trend in SSS (Figure 3g). This sTA and SSS variation, connected to variability in the boundary conditions and a negative trend in precipitation minus evaporation (Figure S4), largely vanished in the CLM_FORC experiment (Figures 3j and 3k).

On the northern GoM shelf, the average OA indicators trends in the climatological experiments displayed the same sign than in the hindcast run but with a greater magnitude (Figure 4; Table S3). River runoff had a much stronger impact on Ω_{Ar} than on pCO_2 or pH. This was mostly related to the variable's sensitivity to changes in TA and DIC. Ω_{Ar} is slightly more responsive to changes in TA than DIC, whereas pCO_2 and pH are more responsive to changes in DIC than TA (Table S4). Consequently, the DIC-driven changes counteracted to a greater degree the TA-driven changes in the cases of pCO_2 and pH. For other coastal regions and the open GoM, the climatological experiments produced relatively weak trend changes in the OA indicators. At the basin level, the effect of river runoff contributed to reduce the pCO_2, pH, and Ω_{Ar} trends by 5%, 6%, and 10%, respectively, while the effect of climate variability contributed to reduce the same trends by 2%, 3%, and 19%, respectively (Figure S5; Table S3). Note that the removal of the surface warming trend in the CLM_FORC experiment (Figure 3l) lessened the growth of pCO_2 and the decline of pH, which explained why the strongest pCO_2 and pH trends were obtained by CLM_RIV rather than CLM_FORC.

4 Discussion

High-resolution ocean models are valuable tools to describe OA trends, particularly in the absence of long-term carbon chemistry time-series. In open GoM waters, our model outputs showed surface trends of 1.59 ± 0.02 μatm yr^{-1}, –0.0016 ± 0.0000 yr^{-1}, and –0.0093 ± 0.0001 yr^{-1} for the mean pCO_2, pH, and Ω_{Ar} anomalies from 1981-2014, respectively. These values are close to previous estimations for subtropical waters in the North Atlantic (Table S5). Along the coastal margins of the GoM, our model revealed significant variations in the OA trend. Estimated shelf averages for the four shelves (Figure 1f) ranged from 1.31 to 1.70 μatm yr^{-1} for pCO_2, from –0.0013 to –0.0017 yr^{-1} for pH, and from –0.0042 to –0.0094 yr^{-1} for Ω_{Ar}. For 1996-2018, Kealoha

et al. (2020) reported mean pCO_2 trends of 3.20 ± 1.47 μatm yr^{-1} and 0.08 ± 1.66 on the western and central parts of the northern GoM shelf, and 2.35 ± 0.82 μatm yr^{-1} on the West Florida shelf. The large trend discrepancies between their estimates and ours are most likely due to the limited spatiotemporal coverage of the pCO_2 datasets used by Kealoha et al. (2020), mostly based on underway ship measurements. This limited coverage, added to the large interannual carbon chemistry variability driven by the MARS runoff, determined a large uncertainty to their long-term trend calculations. This also applies to the very strong pCO_2 trend reported in Robbins et al. (2018) for the West Florida shelf (4.37 μatm yr^{-1}).

Although it is expected that CO_2 in the ocean follows the atmospheric CO_2 growth, multiple studies have shown differences between the ocean and atmospheric CO_2 trends, as interannual and interdecadal variability can exert a significant impact on the ocean sink and pCO_2 trend trajectories (McKinley et al., 2020; Bates & Johnson, 2020). Our model results showed that the basin-averaged pCO_2 trend for 1981-2014 was 7% smaller than the historic atmospheric CO_2 trend. Once we removed the effect associated with river runoff in the CLM_RIV experiment, the difference was insignificant (1%). The positive sTA trend had a significant impact on the three OA indicators examined, contributing to lessen OA progression. The largest sTA increase was on the northern GoM shelf associated with MARS chemistry changes, but the model also exhibited positive sTA trends over the open GoM that were not connected to the coastal sTA signature. This result was consistent with observational studies documenting significant alkalinity growth in the subtropical north Atlantic during the last decades (Bates et al., 2014; Bates & Johnson, 2020; Fine et al., 2017). Besides the sTA growth, the model simulated positive trends for SSS and SST. Surface pCO_2 and pH were especially sensitive to SST changes, with surface warming contributing to accentuate the pCO_2 and pH magnitude in trends.

The MARS is a key driver of hydrographic and biogeochemical patterns on the northern GoM shelf. Multiple studies have reported its influence on salinity, coastal circulation, plankton production, nutrients, dissolved oxygen, and carbon chemistry (e.g., Dagg & Breed, 2003; Rabalais et al., 2007; Lohrenz et al., 2012; Huang et al., 2015). Our study adds another aspect to the impact of the MARS runoff, showing that increasing trends in the river alkalinity had a strong buffering effect nearshore. A sensitivity analysis using climatological forced experiments indicated that changes in MARS chemistry accounted for a 42% reduction in the mean surface Ω_{Ar} trend magnitude over the northern GoM shelf. Changes in river discharge further reduced this Ω_{Ar} trend

magnitude by 8%. Although the potential for watershed export changes to counteract OA patterns has been long recognized (Provoost et al., 2010; Duarte et al., 2013; Montagna et al., 2018), previous OA studies on the northern GoM shelf have mainly focused on the link between coastal eutrophication and subsurface acidification (e.g., Cai et al., 2011), disregarding the effect of riverine alkalinity changes. Quantifying river runoff impacts on OA trends is difficult due to the lack of observations to describe historical river chemistry changes. We could only prescribe time-evolving TA, DIC, and nutrients concentration for the MARS, which accounts for 80% of the total river discharge in the northern GoM, and climatological TA, DIC, and nutrients for other rivers. Thus, the potential impacts linked to secular chemistry changes in small rivers have not been accurately represented. Although acidification has been suggested for Texas rivers (Hu et al., 2015) several studies have shown that the dominant pattern for the U.S. rivers is alkalinization, linked to agriculture practices such as changes in water fluxes and liming (e.g., Raymond et al., 2008; Kaushal et al., 2013; Stets et al., 2014). Therefore, we could expect that carbon-chemistry trends in small rivers would mostly contribute to strengthening, at a local scale, the simulated sTA trend driven by MARS runoff.

5 Conclusions

Our model results showed significant long-term changes in carbon system patterns across the GoM mainly driven by an increase in atmospheric CO_2. The simulated basin-average patterns in the open GoM were consistent with observational studies of OA in subtropical North Atlantic waters. However, a slow OA progression was found on the northern GoM shelf, associated with a significant increase in sTA. The large sTA trend over the northern GoM shelf was mainly due to a positive trend in MARS alkalinity, and secondarily due to the declining discharge trends of low alkalinity rivers. Our study shows the interplay of multiple processes influencing carbon system variability.

Acknowledgments

This article was supported by the NOAA's Ocean Acidification Program and NOAA's Atlantic Oceanographic and Meteorological Laboratory. The research was conducted under NOAA's awards to the Cooperative Institute for Marine and Atmospheric Studies (NA15OAR4320064), and the Northern Gulf Institute (361461-191001-021000). We thank Jay Harris for his kind

assistance with the model experiments, and Emily Osbourne and Gail Derr for their careful manuscript review.

Data Availability Statement

The model outputs used in this study are provided as supplementary information for peer review purposes. Model outputs will be made available in a NOAA repository. The USGS datasets, the ERA-interim reanalysis product, and the atmospheric CO_2 time-series at Mauna Loa Observatory were obtained at https://waterdata.usgs.gov/nwis/inventory/, https://apps.ecmwf.int/datasets/data/interim-full-daily/levtype=sfc/; and https://gml.noaa.gov/webdata/ccgg/trends/co2/co2_mm_mlo.txt, respectively.

References

Bates, N. R., Astor, Y. M., Church, M. J., Currie, K., Dore, J. E., González-Dávila, M., et al. (2014). A time-series view of changing ocean chemistry due to ocean uptake of anthropogenic CO_2 and ocean acidification. *Oceanography*, 27(1): 126–141.

Bates, N. R., & Johnson, R. J. (2020). Acceleration of ocean warming, salinification, deoxygenation and acidification in the surface subtropical North Atlantic Ocean. *Communications Earth & Environment*, *1*(1), 1–12.

Busch, D. S., Bennett-Mintz, J. M., Armstrong, C. T., Jewett, E. B., Gledhill, D. K., & Ombres, E. H. (2018). NOAA Ocean Acidification Program: Taking Stock and Looking Forward, A summary of the 2017 Principal Investigators' Meeting. U.S. Dept. of Commerce, *NOAA Technical Memorandum OAR-OAP-1*, 50 p.

Cai, W. J., Hu, X., Huang, W. J., Murrell, M. C., Lehrter, J. C., Lohrenz, S. E., et al. (2011). Acidification of subsurface coastal waters enhanced by eutrophication. *Nature geoscience*, *4*(11), 766–770.

Cross, J. N., Turner, J. A., Cooley, S. R., Newton, J. A., Azetsu-Scott, K., Chambers, R. C., et al. (2019). The Knowledge-to-Action Pipeline: Connecting Ocean Acidification Research and Actionable Decision Support. *Frontiers in Marine Science*, *6*, p.356.

Dagg, M. J. & Breed, G. A. (2003). Biological effects of Mississippi River nitrogen on the northern Gulf of Mexico–a review and synthesis. *J. Mar. Syst.*, *43*(3-4), 133–152.

Damien, P., Pasqueron de Fommervault, O., Sheinbaum, J., Jouanno, J., Camacho-Ibar, V. F., &

Duteil, O. (2018). Partitioning of the open waters of the Gulf of Mexico based on the seasonal and interannual variability of chlorophyll concentration. *J. Geophys. Res.-Oceans*, *123*(4), 2592–2614.

Dee, D. P., Uppala, S. M., Simmons, A. J., Berrisford, P., Poli, P., Kobayashi, S., et al. (2011). The ERA-Interim reanalysis: configuration and performance of the data assimilation system. *Q. J. Roy. Meteor. Soc.,* 137, 553–597.

Doney, S. C., Busch, D. S., Cooley, S. R., & Kroeker, K. J. (2020). The Impacts of Ocean Acidification on Marine Ecosystems and Reliant Human Communities. *Annual Review of Environment and Resources, 45:*83–112.

Doney, S. C., Fabry, V. J., Feely, R. A., & Kleypas, J. A. (2009). Ocean acidification: the other CO2 problem. *Annu. Rev. Mar. Sci.,* 1, 169–92.

Duarte, C. M., Hendriks, I. E., Moore, T. S., Olsen, Y. S., Steckbauer, A., Ramajo, L., et al. (2013). Is ocean acidification an open-ocean syndrome? Understanding anthropogenic impacts on seawater pH. *Estuaries and Coasts*, *36*(2), 221-236.

Ekstrom, J. A., Suatoni, L., Cooley, S. R., Pendleton, L. H., Waldbusser, G. G., Cinner, J. E., et al. (2015). Vulnerability and adaptation of US shellfisheries to ocean acidification. *Nature Climate Change*, *5*(3), 207–214.

Fine, R. A., Willey, D. A., & Millero, F. J. (2017). Global variability and changes in ocean total alkalinity from Aquarius satellite data. *Geophysical Research Letters*, *44*(1), 261–267.

Gledhill, D. K., Wanninkhof, R., Millero, F. J., & Eakin, M. (2008). Ocean acidification of the greater Caribbean region 1996–2006. *J. Geophys. Res.-Oceans*, *113*(C10).

Gomez, F. A., Lee, S. K., Liu, Y., Hernandez Jr, F. J., Muller-Karger, F. E., & Lamkin, J. T. (2018). Seasonal patterns in phytoplankton biomass across the northern and deep Gulf of Mexico: a numerical model study, *Biogeosciences*, 15, 3561–3576.

Gomez, F. A., Wanninkhof, R., Barbero, L., Lee, S. K., & Hernandez, F. J. (2020). Seasonal patterns of surface inorganic carbon system variables in the Gulf of Mexico inferred from a regional high-resolution ocean biogeochemical model, *Biogeosciences*, 17, 1685–1700.

Gruber, N., Clement, D., Carter, B. R., Feely, R. A., Van Heuven, S., Hoppema, M., et al. (2019). The oceanic sink for anthropogenic CO_2 from 1994 to 2007. *Science*, *363*(6432), 1193-1199.

He, B., Kanae, S., Oki, T., Hirabayashi, Y., Yamashiki, Y., & Takara, K. (2011). Assessment of global nitrogen pollution in rivers using an integrated biogeochemical modeling framework.

Water Res., 45, 2573–2586.

Hoegh-Guldberg, O., Mumby, P. J., Hooten, A. J., Steneck, R. S., Greenfield, P., Gomez, E., et al. (2007). Coral reefs under rapid climate change and ocean acidification. *Science*, *318*(5857), 1737–1742.

Hu, X., Nuttall, M. F., Wang, H., Yao, H., Staryk, C. J., McCutcheon, M. R., et al. (2018). Seasonal variability of carbonate chemistry and decadal changes in waters of a marine sanctuary in the Gulf of Mexico. *Marine Chemistry*, 205, 16–28.

Hu, X., Pollack, J. B., McCutcheon, M. R., Montagna, P. A., & Ouyang, Z. (2015). Long-term alkalinity decrease and acidification of estuaries in northwestern Gulf of Mexico. *Environmental science & technology*, *49*(6), 3401–3409.

Huang, W. J., Cai, W. J., Wang, Y., Lohrenz, S. E., & Murrell, M. C. (2015). The carbon dioxide system on the Mississippi River‐dominated continental shelf in the northern Gulf of Mexico: 1. Distribution and air‐sea CO2 flux. *J. Geophys. Res.-Oceans*, *120*(3), 1429–1445.

Kaushal, S. S., Likens, G. E., Utz, R. M., Pace, M. L., Grese, M., & Yepsen, M. (2013). Increased river alkalinization in the Eastern US. *Environmental science & technology*, *47*(18), 10302–10311.

Kealoha, A. K., Shamberger, K. E., DiMarco, S. F., Thyng, K. M., Hetland, R. D., Manzello, D. P., et al. (2020). Surface Water CO_2 variability in the Gulf of Mexico (1996–2017). *Scientific reports*, *10*(1), 1–13.

Laruelle, G. G., Cai, W. J., Hu, X., Gruber, N., Mackenzie, F. T., & Regnier, P. (2018). Continental shelves as a variable but increasing global sink for atmospheric carbon dioxide. *Nature communications*, *9. 454.*

Lauvset, S. K., Gruber, N., Landschützer, P., Olsen, A., & Tjiputra, J. F. Trends and drivers in global surface ocean pH over the past 3 decades. *Biogeosciences*, *12*(5), 1285–1298 (2015).

Liu, Y., Lee, S. K., Enfield, D. B., Muhling, B. A., Lamkin, J. T., Muller-Karger, F. E., & Roffer, M. A. (2015). Potential impact of climate change on the Intra-Americas Sea: Part-1, A dynamic downscaling of the CMIP5 model projections. *J. Mar. Syst.*, 148, 56–69.

Lohrenz, S. E., Cai, W. J., Chakraborty, S., Huang, W. J., Guo, X., He, R., et al. (2018). Satellite estimation of coastal pCO2 and air–sea flux of carbon dioxide in the northern Gulf of Mexico, Remote Sens. Environ., 207, 71–83.

Lohrenz, S. E., Cai, W. J., Chen, F., Chen, X., & Tuel, M. (2010). Seasonal variability in air-sea

fluxes of CO_2 in a river influenced coastal margin. *J. Geophys. Res.-Oceans*, 115, C10034.

Martínez-López, B., & Zavala-Hidalgo, J. (2009). Seasonal and interannual variability of cross-shelf transports of chlorophyll in the Gulf of Mexico. *J. Mar. Syst*., 77, 1–20.

McKinley, G. A., Fay, A. R., Eddebbar, Y. A., Gloege, L., & Lovenduski, N. S. (2020). External forcing explains recent decadal variability of the ocean carbon sink. *AGU Advances*, 1, e2019AV000149.

Montagna, P. A., Hu, X., Palmer, T. A., & Wetz, M. (2018). Effect of hydrological variability on the biogeochemistry of estuaries across a regional climatic gradient. *Limnol. Oceanogr*., *63*(6), 2465–2478.

Muller-Karger, F. E., Smith, J. P., Werner, S., Chen, R., Roffer, M., Liu, Y., et al. (2015). Natural variability of surface oceanographic conditions in the offshore Gulf of Mexico. *Progress in Oceanography*, *134*, 54–76.

Muñoz-Salinas, E. & Castillo, M. (2015). Streamflow and sediment load assessment from 1950 to 2006 in the Usumacinta and Grijalva Rivers (Southern Mexico) and the influence of ENSO. *Catena*, 127, 270–278.

Provoost, P., Van Heuven, S., Soetaert, K., Laane, R. W. P. M., & Middelburg, J. J. (2010). Seasonal and long-term changes in pH in the Dutch coastal zone, *Biogeosciences*, *7*(11), 3869–3878.

Rabalais, N. N., Turner, R. E., Gupta, B. S., Boesch, D. F., Chapman, P., & Murrell, M. C. (2007). Hypoxia in the northern Gulf of Mexico: Does the science support the plan to reduce, mitigate, and control hypoxia?. *Estuaries and Coasts*, *30*(5), 753–772.

Raymond, P. A., Oh, N. H., Turner, R. E., & Broussard, W. (2008). Anthropogenically enhanced fluxes of water and carbon from the Mississippi River. *Nature*, *451*(7177), 449–452.

Robbins, L. L., Daly, K. L., Barbero, L., Wanninkhof, R., He, R., Zong, H., et al. (2018). Spatial and temporal variability of pCO_2, carbon fluxes and saturation state on the West Florida Shelf. *J. Geophys. Res.-Oceans*, 123.

Salisbury, J. E., & Jönsson, B. F. (2018). Rapid warming and salinity changes in the Gulf of Maine alter surface ocean carbonate parameters and hide ocean acidification. *Biogeochemistry*, *141*(3), 401–418.

Shchepetkin, A. F., & McWilliams, J. C. (2005). The regional oceanic modeling system (ROMS): a split-explicit, free-surface, topography-following-coordinate oceanic model. *Ocean Model*.,

9, 347–404.

Stets, E. G., Kelly, V. J., & Crawford, C. G. (2014). Long-term trends in alkalinity in large rivers of the conterminous US in relation to acidification, agriculture, and hydrologic modification. *Sci. Total Environ*., 488, 280–289.

Turi, G., Lachkar, Z., Gruber, N., & Münnich, M. (2016). Climatic modulation of recent trends in ocean acidification in the California Current System, *Environmental Research Letters*, *11*(1), p.014007.

van Heuven, S. M. A. C., Pierrot, D., Rae, J. W. B., Lewis E., & Wallace D. W. R. (2011). MATLAB program developed for CO2 system calculations. ORNL/CDIAC-105b. Carbon Dioxide Information Analysis Center, Oak Ridge National Laboratory, US Department of Energy, Oak Ridge, Tennessee, 530.

Waldbusser, G. G., Hales, B., Langdon, C. J., Haley, B. A., Schrader, P., Brunner, E. L., et al. (2015). Saturation-state sensitivity of marine bivalve larvae to ocean acidification. *Nature Climate Change*, *5*(3), 273–280.

Wang, Z. A., Wanninkhof, R., Cai, W. J., Byrne, R. H., Hu, X., Peng, T. H., & Huang, W. J. (2013). The marine inorganic carbon system along the Gulf of Mexico and Atlantic coasts of the United States: Insights from a transregional coastal carbon study. *Limnol. Oceanogr*., 58, 325–342.

Wanninkhof, R., Barbero, L., Byrne, R., Cai, W. J., Huang, W. J., Zhang, J. Z., et al. (2015). Ocean acidification along the Gulf Coast and East Coast of the USA. *Continental Shelf Research*, 98, 54–71.

Wanninkhof, R., Trinanes, J., Park, G.-H., Gledhill, D., & Olsen, A. (2019). Large decadal changes in air-sea CO_2 fluxes in the Caribbean Sea. Journal of Geophysical Research: Oceans, 124, 6960–6982, https://doi.org/10.1029/2019JC015366

Xu, Y. Y., Cai, W. J., Wanninkhof, R., Salisbury, J., Reimer, J., & Chen, B. (2020). Long-term changes of carbonate chemistry variables along the north American East Coast. *J. Geophys. Res.-Oceans: Oceans*, *125*(7), 2019JC015982.

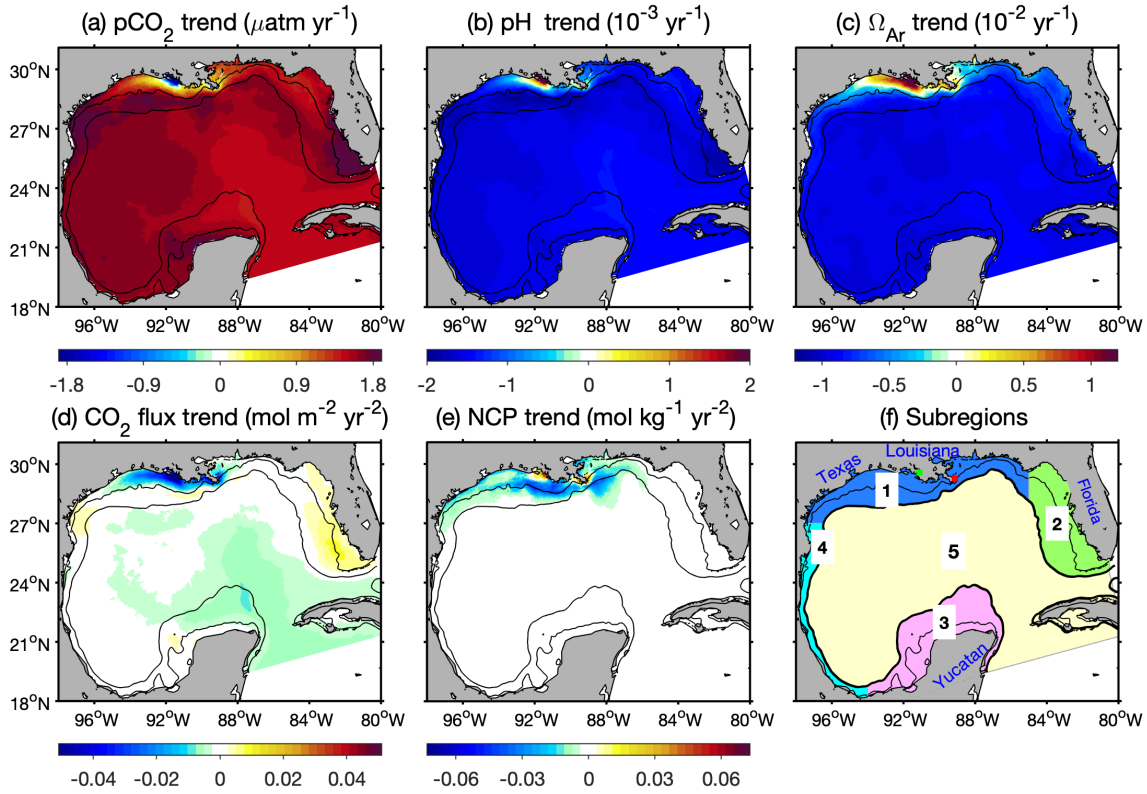

Figure 1. Surface trends of **(a)** partial pressure of CO_2, **(b)** pH, **c)** aragonite saturation state, **(d)** air-sea CO_2 flux, and **(e)** net community production derived from the model hindcast. **(f)** Areas used to derive subregional trend patterns: (1) northern GoM shelf; (2) West Florida shelf; (3) Yucatan shelf; (4) western GoM shelf; and (5) open GoM. Red and green dots in (f) depict the Mississippi and Atchafalaya mouths, respectively. Negative CO_2 flux trend implies increasing carbon uptake. Black contours depict the 25 and 200 m isobaths. The 25 m isobath defines the limit between the inner and outer shelf.

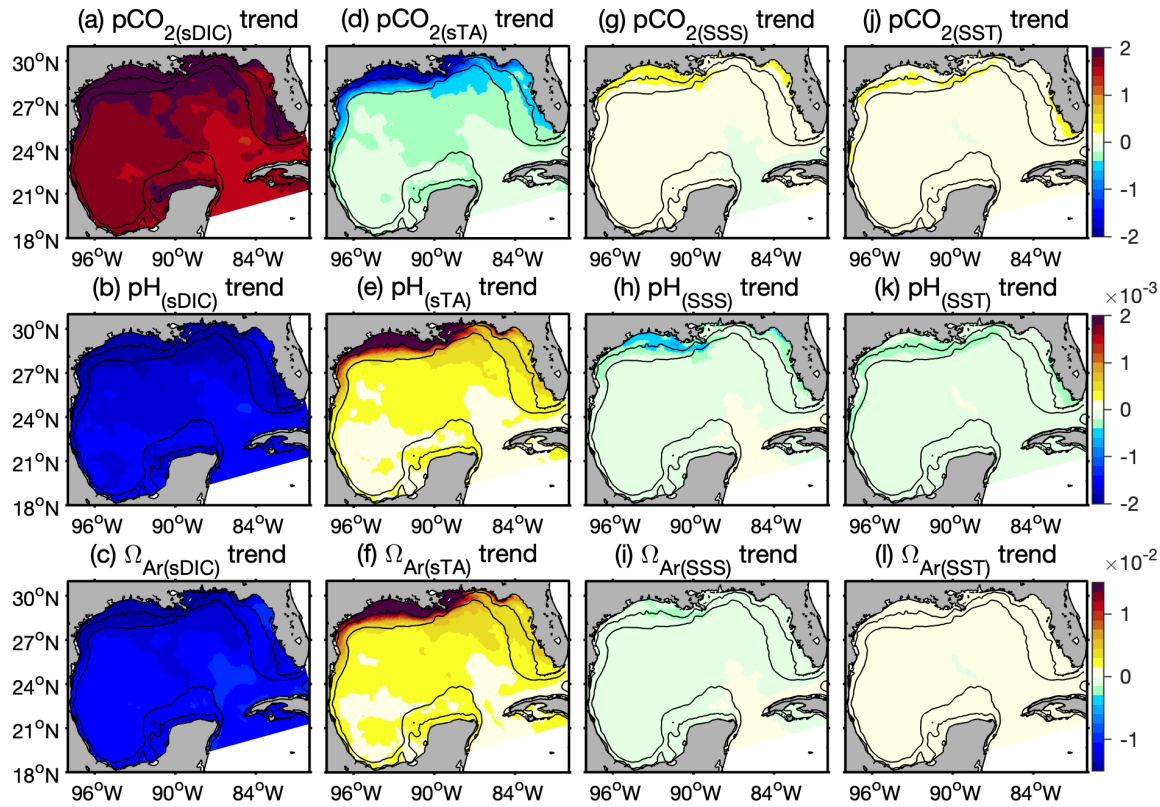

Figure 2. Taylor series decomposition of the surface partial pressure of CO_2 (μatm yr^{-1}; upper panels), surface pH (yr^{-1}; middle panels), and surface aragonite saturation state (yr^{-1}; bottom panels) trends derived from the model hindcast. Patterns terms represent the contribution of **(a–c)** surface dissolved inorganic carbon (sDIC); **(d–f)** surface total alkalinity (sTA); **(g–i)** sea surface salinity (SSS); and **(j–l)** sea surface temperature (SST). Black contours depict the 25 and 200 m isobaths.

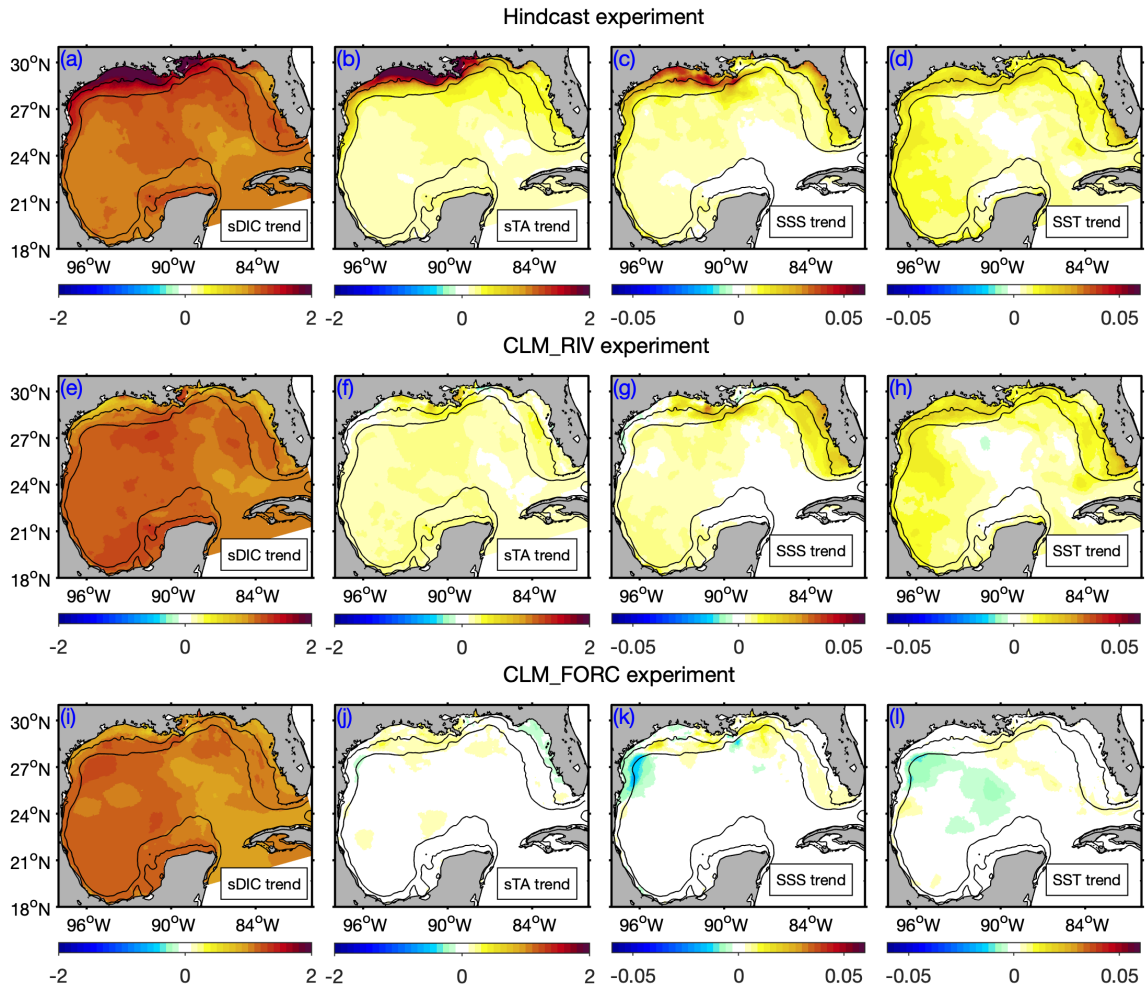

Figure 3. Trends of surface dissolved inorganic carbon (sDIC), surface total alkalinity (sTA), sea surface salinity (SSS), and sea surface temperature (SST) as derived from the **(a–d)** hindcast, (**e–h)** climatological rivers (CLM_RIV), and (**i–l)** climatological forcing (CLM_FORC) experiments. Trends for sDIC and sTA are in μmol kg^{-1} yr^{-1}, for SSS in yr^{-1}, and for SST in °C yr^{-1}. Black contours depict the 25 and 200 m isobaths.

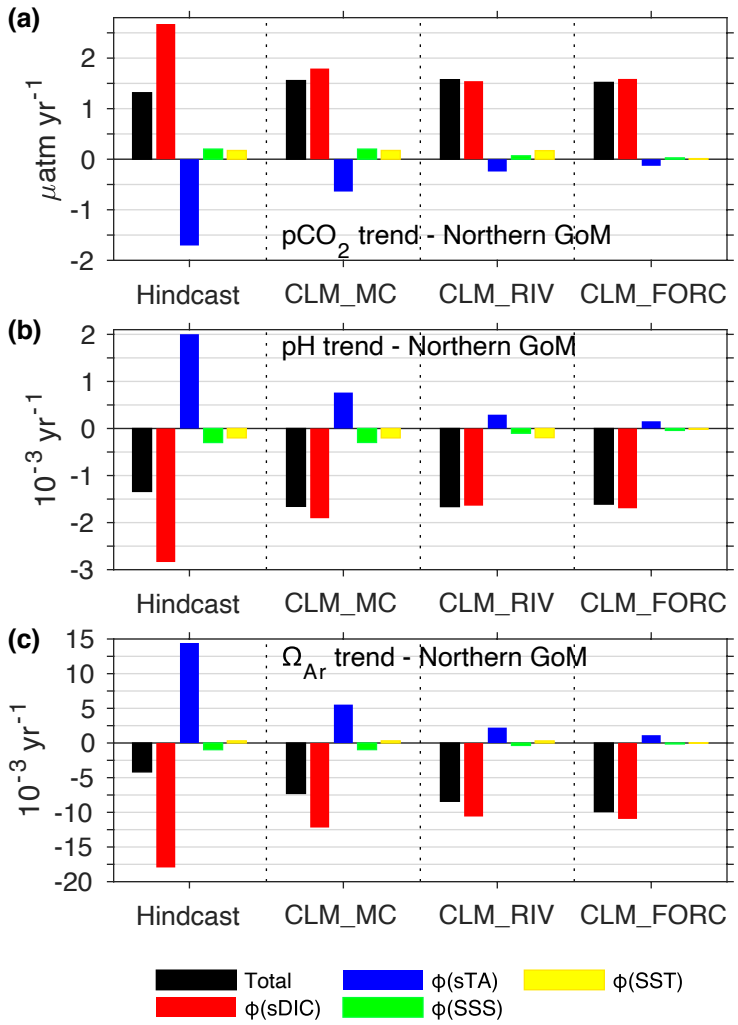

Figure 4. Trend decomposition of ocean acidification indicators over the northern GoM shelf derived from the hindcast, CLM_MC, CLM_RIV, and CLM_FORC experiments: (**a**) partial pressure of CO_2 (**p**CO_2), (**b**) pH, and (**c**) aragonite saturation state (Ω_{Ar}**).** Red, blue, green, and yellow bars represent the contribution of surface dissolved inorganic carbon (sDIC), surface total alkalinity (sTA), sea surface salinity (SSS), and sea surface temperature (SST) to the total trend (in black), respectively.

Geophysical Research Letters

Supporting Information for

Increasing river alkalinity slows ocean acidification in the northern Gulf of Mexico

Fabian A. Gomez[1,2], Rik Wanninkhof[2], Leticia Barbero[3,2], Sang-Ki Lee[2]

[1] Northern Gulf Institute, Mississippi State University, Starkville, Mississippi, USA
[2] NOAA Atlantic Oceanographic and Meteorological Laboratory, Miami, Florida, USA
[3] Cooperative Institute for Marine and Atmospheric Studies, University of Miami, Miami, Florida, USA

Contents of this file

Figures S1 to S5
Tables S1 to S5

Additional Supporting Information

Datasets S1 to S29

Introduction

The following figures and tables provide complementary information to the main manuscript.

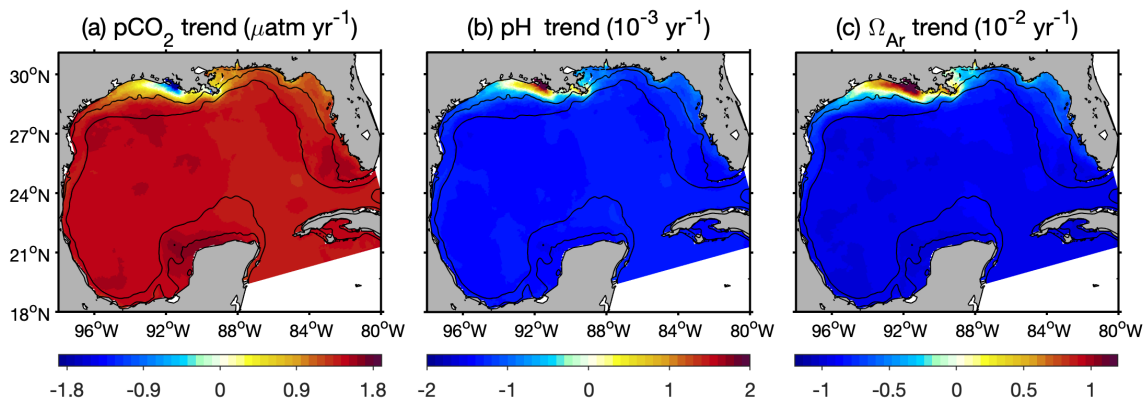

Figure S1. Trend patterns for (a) partial pressure of CO_2 (pCO_2), (b) pH, and (c) aragonite saturation state (Ω_{Ar}) after removing the salinity and temperature effect. Black contours depict the 25 and 200 m isobaths.

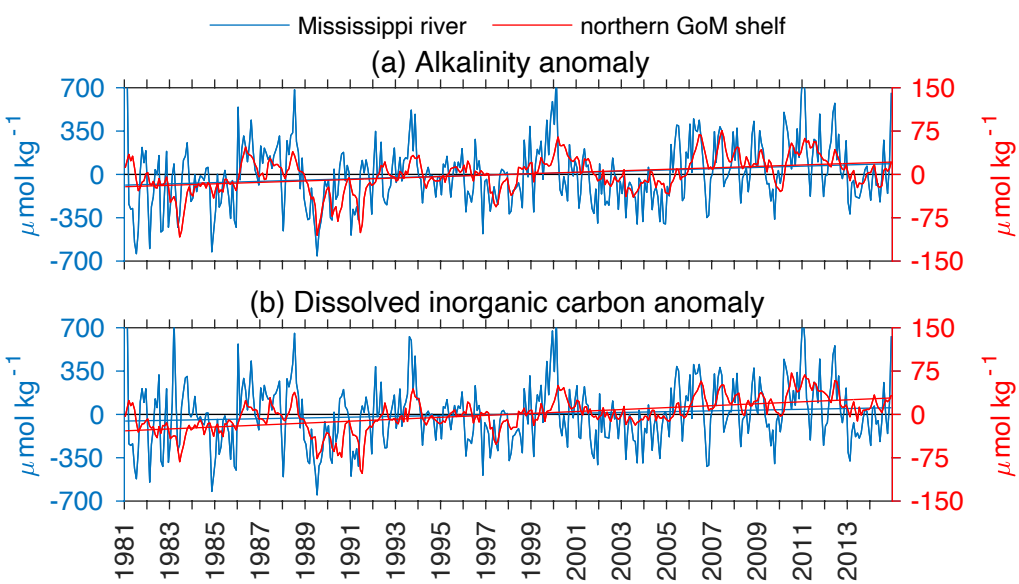

Figure S2. Mississippi river and northern GoM shelf patterns in carbonate chemistry. Low frequency patterns for (a) alkalinity and (b) dissolved inorganic carbon in the Mississippi river and the surface layer of the northern GoM shelf.

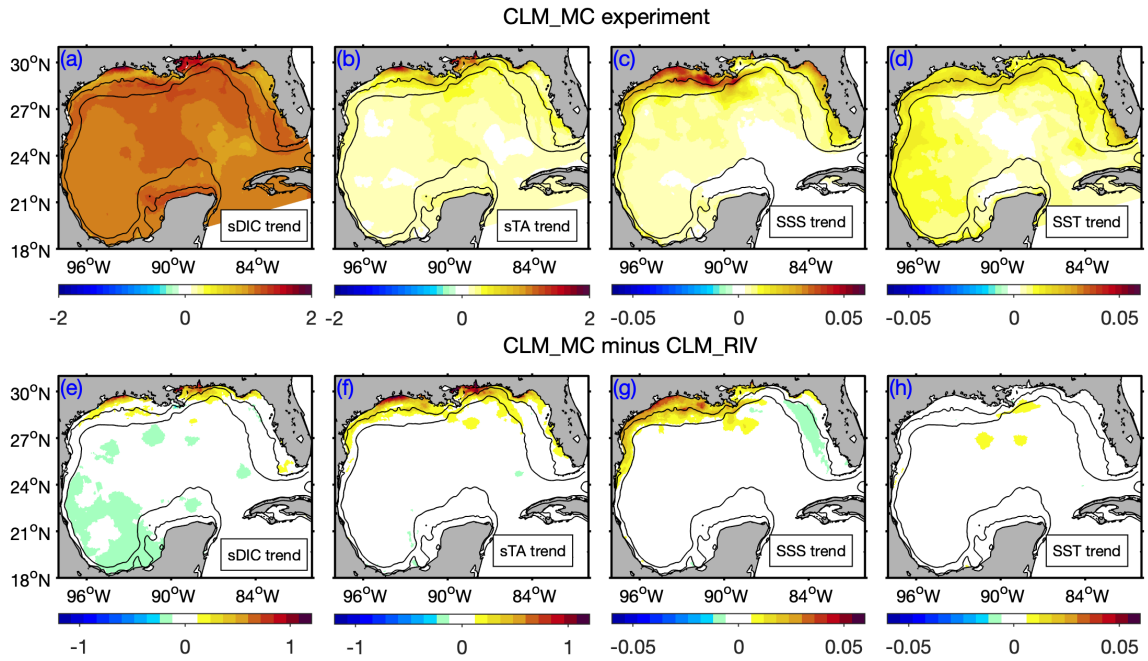

Figure S3. (a–d) Trend patterns for surface dissolved inorganic carbon (sDIC), surface total alkalinity (sTA), sea surface salinity (SSS), and sea surface temperature (SST) derived from climatological MARS chemistry experiment (CLM_MC); (e–h) Differences between trend patterns from CLM_MC and climatological river experiment (CLM_RIV). Trends for sDIC and sTA are in μmol kg^{-1} yr^{-1}, for SSS in yr^{-1}, and for SST in °C yr^{-1}. Black contours depict the 25 and 200 m isobaths.

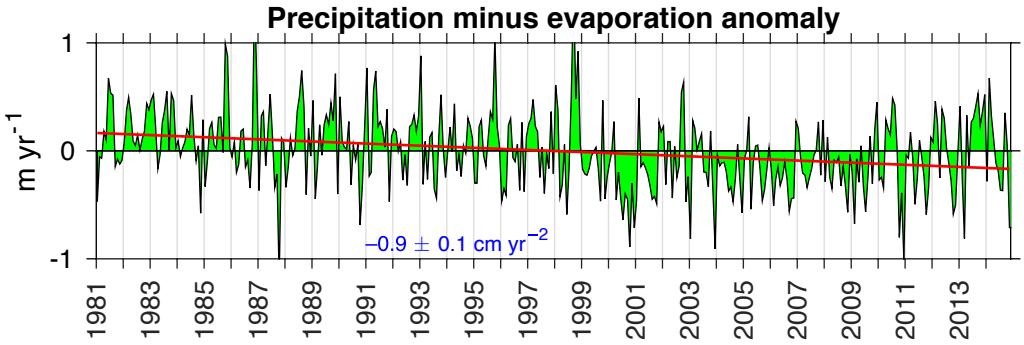

Figure S4. Average time series of precipitation minus evaporation anomaly across the Gulf of Mexico. Red line depicts the linear regression for 1981–2014. Long-term trend is indicated in blue.

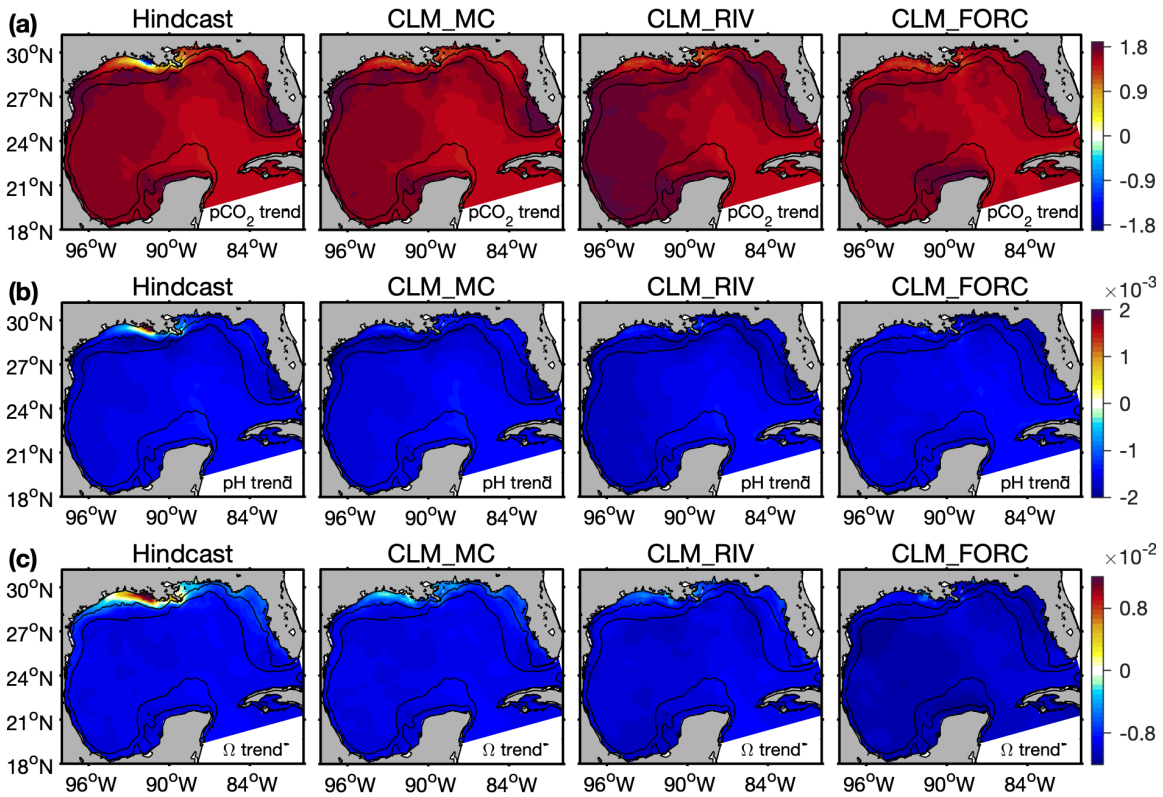

Figure S5. Sensitivity analysis for the simulated ocean acidification indicator's trends: (a) partial pressure of CO_2 trend (μatm yr^{-1}), (b) pH trend (yr^{-1}), and (c) aragonite saturation state trend (yr^{-1}) derived from the model hindcast, climatological MARS chemistry experiment (CLM_MC), climatological rivers experiment (CLM_RIV), and climatological forcing experiment (CLM_FORC). Black contours depict the 25 and 200 m isobaths.

	SST trend [10^{-3} °C yr^{-1}]	SSS trend [10^{-3} yr^{-1}]	sTA trend [µmol kg^{-1} yr^{-1}]	sDIC trend [µmol kg^{-1} yr^{-1}]	pCO_2 trend [µatm yr^{-1}]	pH trend [10^{-3} yr^{-1}]	Ω_{Ar} trend [10^{-3} yr^{-1}]	CO_2 flux trend [mmol m^{-2} yr^{-2}]
GoM basin	7.93 (2.02)	6.63 (0.90)	0.31 (0.02)	1.16 (0.02)	1.57 (0.03)	–1.53 (0.03)	–8.66 (0.15)	–3.68 (0.95)
1. Northern GoM shelf	13.98 (3.42)	22.09 (4.66)	1.26 (0.14)	1.67 (0.11)	1.31 (0.07)	–1.34 (0.08)	–4.18 (0.57)	–9.18 (2.74)
Inner shelf	13.92 (4.16)	27.32 (6.60)	1.90 (0.22)	1.97 (0.17)	0.93 (0.10)	–0.94 (0.11)	–0.26* (0.85)	–17.61 (2.79)
Outer shelf	14.02 (2.99)	18.05 (3.63)	0.76 (0.08)	1.45 (0.07)	1.61 (0.06)	–1.64 (0.07)	–7.18 (0.43)	–2.69* (1.80)
2. West Florida shelf	10.69 (3.73)	10.55 (1.91)	0.32 (0.03)	1.12 (0.02)	1.64 (0.05)	–1.59 (0.05)	–8.21 (0.29)	2.38* (1.51)
Inner shelf north 27ºN	8.93 (5.02)	21.57 (3.74)	0.43 (0.06)	1.03 (0.04)	1.55 (0.08)	–1.48 (0.08)	–6.57 (0.40)	1.78* (1.92)
Inner shelf south 27ºN	17.59 (4.56)	13.30 (2.09)	0.32 (0.09)	1.15 (0.03)	1.87 (0.07)	–1.78 (0.07)	–8.62 (0.46)	4.86 (1.48)
Outer shelf	9.32 (3.22)	5.75 (1.67)	0.31 (0.03)	1.14 (0.03)	1.61 (0.03)	–1.58 (0.04)	–8.69 (0.25)	1.88* (1.50)
3. Yucatan shelf	5.32 (2.19)	2.28 (0.57)	0.17 (0.02)	1.09 (0.02)	1.59 (0.03)	–1.51 (0.03)	–9.37 (0.16)	–3.53 (0.91)
Inner shelf	6.22 (2.64)	3.26 (0.87)	0.19 (0.02)	1.13 (0.02)	1.69 (0.04)	–1.57 (0.04)	–9.60 (0.18)	–1.16* (0.93)
Outer shelf	4.97 (2.06)	1.91 (0.52)	0.16 (0.02)	1.08 (0.02)	1.56 (0.03)	–1.49 (0.03)	–9.28 (0.15)	–4.43 (0.93)
4. Western GoM shelf	12.56 (2.44)	10.21 (2.83)	0.32 (0.05)	1.17 (0.03)	1.70 (0.04)	–1.67 (0.04)	–8.77 (0.27)	–0.96* (1.05)
5. Open GoM	6.85 (1.81)	4.27 (0.62)	0.19 (0.02)	1.10 (0.02)	1.59 (0.02)	–1.55 (0.02)	–9.30 (0.12)	–3.79 (0.89)

Table S1. Simulated trends for carbon system variables in the Gulf of Mexico (GoM) and sub-regions as derived from the hindcast experiment (1981-2014): sea surface temperature (SST), sea surface salinity (SSS), surface total alkalinity (sTA), surface dissolved inorganic carbon (sDIC), surface partial pressure of CO_2 (pCO_2), surface pH, surface aragonite saturation state (Ω_{Ar}), and air–sea CO_2 flux. Standard errors are indicated in parenthesis. Main subregions are depicted in Fig. 1c. The northern GoM, West Florida, and Yucatan shelves were divided in inner and outer part (bottom depths 0-25 m and 25-200 m, respectively). Florida inner shelf was further divided in a northern and a southern part. (*) Non-significant trend at the 95% confidence level.

	Mississippi	Atchafalaya
	Mean values (1981-2014)	
DIC (μmol kg^{-1})	2,301 (328)	2,019 (413)
TA (μmol kg^{-1})	2,228 (333)	1,941 (426)
TA:DIC ratio	0.968 (0.029)	0.959 (0.046)
	Linear trends (1981-2014)	
DIC trend (μmol kg^{-1} yr^{-1})	3.2 (1.3)	3.0 (1.6)
TA trend (μmol kg^{-1} yr^{-1})	5.1 (1.2)	5.6 (1.6)
TA:DIC ratio trend (yr^{-1})	0.88×10^{-3} (0.14×10^{-3})	1.37×10^{-3} (0.21×10^{-3})

Table S2. Long term patterns for the Mississippi and Atchafalaya carbon chemistry derived from the U.S. Geological Survey records. Standard errors of the mean values and trends are indicated in parenthesis.

	SST [10^{-3} °C yr^{-1}]	SSS [10^{-3} yr^{-1}]	sTA [μmol kg^{-1} yr^{-1}]	sDIC [μmol kg^{-1} yr^{-1}]	pCO_2 [μatm yr^{-1}]	pH [10^{-3} yr^{-1}]	Ω_{Ar} [10^{-3} yr^{-1}]
CLM_MC experiment							
GoM basin	7.9 (1.00)	6.6 (1.00)	0.20 (0.65)	1.09 (0.93)	1.60 (1.02)	–1.57 (1.03)	–9.11 (1.05)
Northern GoM shelf	14.0 (1.00)	22.1 (1.00)	0.49 (0.39)	1.14 (0.68)	1.56 (1.19)	–1.65 (1.23)	–7.28 (1.74)
West Florida shelf	10.7 (1.00)	10.6 (1.00)	0.24 (0.75)	1.07 (0.96)	1.66 (1.01)	–1.62 (1.02)	–8.55 (1.04)
Yucatan shelf	5.3 (1.00)	2.3 (1.00)	0.17 (1.00)	1.09 (1.00)	1.59 (1.00)	–1.51 (1.00)	–9.39 (1.00)
Western GoM shelf	12.6 (1.00)	10.2 (1.00)	0.19 (0.59)	1.07 (0.91)	1.71 (1.01)	–1.71 (1.02)	–9.23 (1.05)
Open GoM	6.9 (1.00)	4.3 (1.00)	0.16 (0.84)	1.08 (0.98)	1.59 (1.00)	–1.56 (1.01)	–9.41 (1.01)
CLM_RIV experiment							
GoM basin	7.4 (0.93)	4.9 (0.74)	0.18 (0.58)	1.11 (0.96)	1.65 (1.05)	–1.62 (1.05)	–9.57 (1.11)
Northern GoM shelf	13.7 (0.98)	7.5 (0.34)	0.20 (0.16)	1.00 (0.60)	1.57 (1.20)	–1.66 (1.23)	–8.41 (2.01)
West Florida shelf	11.8 (1.10)	14.3 (1.34)	0.20 (0.62)	1.04 (0.93)	1.74 (1.06)	–1.71 (1.08)	–8.94 (1.08)
Yucatan shelf	4.0 (0.75)	2.7 (1.17)	0.21 (1.23)	1.17 (1.07)	1.67 (1.05)	–1.57 (1.04)	–9.87 (1.05)
Western GoM shelf	11.8 (0.95)	4.1 (0.40)	0.16 (0.50)	1.14 (0.97)	1.79 (1.05)	–1.76 (1.05)	–9.98 (1.14)
Open GoM	6.2 (0.89)	3.7 (0.87)	0.17 (0.89)	1.13 (1.03)	1.64 (1.03)	–1.60 (1.03)	–9.78 (1.05)
CLM_FORC experiment							
GoM basin	0.1 (0.01)	0.6 (0.09)	0.04 (0.13)	1.06 (0.91)	1.61 (1.03)	–1.57 (1.03)	–10.66 (1.23)
Northern GoM shelf	1.5 (0.11)	2.7 (0.12)	0.10 (0.08)	1.03 (0.62)	1.51 (1.15)	–1.61 (1.20)	–9.90 (2.37)
West Florida shelf	1.3 (0.12)	2.4 (0.23)	–0.01 (–0.03)	1.03 (0.91)	1.72 (1.05)	–1.67 (1.05)	–10.68 (1.30)
Yucatan shelf	–0.1 (–0.02)	0.5 (0.22)	0.03 (0.17)	1.10 (1.00)	1.68 (1.06)	–1.60 (1.06)	–11.05 (1.18)
Western GoM shelf	0.2 (0.02)	–2.8 (0.27)	0.03 (0.09)	1.12 (0.96)	1.69 (0.99)	–1.63 (0.98)	–11.17 (1.27)
Open GoM	–0.3 (–0.04)	0.3 (0.07)	0.03 (0.16)	1.07 (0.97)	1.59 (1.00)	–1.55 (1.00)	–10.69 (1.15)

Table S3. Simulated surface trends (1981–2014) for sea surface temperature (SST), sea surface salinity (SSS), surface total alkalinity (sTA), surface dissolved inorganic carbon (sDIC), partial pressure of CO_2 (pCO_2), pH, and aragonite saturation state (Ω_{Ar}) derived from the climatological experiments. The ratio between the climatological and hindcast trends is reported in parenthesis.

X:	SST	SSS	sTA	sDIC
$\partial pCO_2/\partial X$	12.9219	8.7166	–1.2253	1.5264
$\partial pH/\partial X$	–0.0150	–0.0130	0.0015	–0.0016
$\partial \Omega/\partial X$	0.0233	–0.0438	0.0112	–0.0106

Table S4. Partial derivatives of partial pressure of CO_2 (CO_2), pH, and aragonite saturation state (Ω_{Ar}) for an average surface condition on the northern GoM shelf during 1981-2014: sea surface temperature (SST) = 24.4°C; sea surface salinity (SSS) = 32.2; surface dissolved inorganic carbon (sDIC) = 1,987 μmol kg^{-1}; surface total alkalinity (sTA) = 2,311μmol kg^{-1}.

	Region	Period	pCO_2 trend ($\mu atm\ yr^{-1}$)	pH trend ($10^{-3}\ yr^{-1}$)	Ω_{Ar} trend ($10^{-3}\ yr^{-1}$)
Open ocean:					
Present study	Open GoM	1981-2014	1.59 ± 0.02	–1.6 ± 0.0	–9.3 ± 0.1
Kealoha et al. (2020)	Open GoM	1996-2018	Ranging from –0.21 ± 0.67 to 1.70 ± 0.14		
Xu et al. (2020)	Offshore South Atlantic Bight	1981-2011	1.38 ± 0.04	–1.3 ± 0.5	–7.3 ± 1.1
Lauvset et al. (2015)	Stratified Subtropical North Atlantic	1991-2011	1.44 ± 0.12	–1.1 ± 0.2	
		1981-2011	1.42 ± 0.12		
Bates et al. (2014)	BATS	1983-2014	1.69 ± 0.11	–1.7 ± 0.1	–9.5 ± 0.7
Bates & Johnson (2020)	BATS	1983-2020	1.92 ± 0.08	–1.9 ± 0.1	–9 ± 1
Wanninkhof et al. (2019)	Caribbean Sea	2002-2018	1.30 ± 0.03		
Gledhill et al. (2008)	Caribbean Sea	1996-2006			–12 ± 1
Coastal regions:					
Present study	GoM shelves	1981-2014	Ranging from 1.31 ± 0.07 to 1.70 ± 0.04	Ranging from –1.3 ± 0.1 to –1.7 ± 0.0	Ranging from –4.2 ± 0.6 to –9.4 ± 0.2
Kealoha et al. (2020)	GoM shelves	1996-2018	Ranging from 0.08 ± 1.66 to 3.20 ± 1.47		
Robbins et al. (2018)	West Florida	1996-2016	4.37		
Xu et al. (2020)	South Atlantic Bight shelf	1981-2011	1.40 ± 0.09	–1.3 ± 0.1	–6.3 ± 1.5
	Mid Atlantic Bight shelf	1981-2011	1.77 ± 0.07	–1.9 ± 0.1	–10.3 ± 1.0

Table S5. Simulated trends and reported trend values for partial pressure of CO_2 (pCO_2), pH, and aragonite saturation state (Ω_{Ar}) in open ocean and coastal regions from the north Atlantic.

Datasets S1 to S7:

Datasets S1 to S7 contain the monthly outputs (January 1981 to December 2014) of sea surface temperature, sea surface salinity, surface alkalinity, surface dissolved inorganic carbon, surface partial pressure of CO_2, surface pH, and surface aragonite saturation state derived from the model hindcast experiment. Each file contains a 3-dimension array (longitude, latitude, time). The horizontal model grid (longitude, latitude) is provided in Dataset S29.

	Variable	**Array name**	**Units**
Dataset S1	Sea surface temperature	SST	°C
Dataset S2	Sea surface salinity	SSS	Unitless
Dataset S3	Surface alkalinity	ALK	$\mu mol\ kg^{-1}$
Dataset S4	Surface dissolved inorganic carbon	DIC	$\mu mol\ kg^{-1}$
Dataset S5	Surface partial pressure of CO_2	PCO2	µatm
Dataset S6	Surface pH	pH	Unitless
Dataset S7	Surface aragonite saturation state	OMar	Unitless

Datasets S8 to S14:

As Datasets S1-S7 but for the climatological river experiment.

	Variable	**Array name**	**Units**
Dataset S8	Sea surface temperature	SST	°C
Dataset S9	Sea surface salinity	SSS	Unitless
Dataset S10	Surface alkalinity	ALK	$\mu mol\ kg^{-1}$
Dataset S11	Surface dissolved inorganic carbon	DIC	$\mu mol\ kg^{-1}$
Dataset S12	Surface partial pressure of CO_2	PCO2	µatm
Dataset S13	Surface pH	pH	Unitless
Dataset S14	Surface aragonite saturation state	OMar	Unitless

Datasets S15 to S21:

As Datasets S1-S7 but for the climatological MARS chemistry experiment.

	Variable	**Array name**	**Units**
Dataset S15	Sea surface temperature	SST	°C
Dataset S16	Sea surface salinity	SSS	Unitless
Dataset S17	Surface alkalinity	ALK	µmol kg^{-1}
Dataset S18	Surface dissolved inorganic carbon	DIC	µmol kg^{-1}
Dataset S19	Surface partial pressure of CO_2	PCO2	µatm
Dataset S20	Surface pH	pH	Unitless
Dataset S21	Surface aragonite saturation state	OMar	Unitless

Datasets S22 to S28:

As Datasets S1-S7 but for the climatological forcing experiment.

	Variable	**Array name**	**Units**
Dataset S22	Sea surface temperature	SST	°C
Dataset S23	Sea surface salinity	SSS	Unitless
Dataset S24	Surface alkalinity	ALK	µmol kg^{-1}
Dataset S25	Surface dissolved inorganic carbon	DIC	µmol kg^{-1}
Dataset S26	Surface partial pressure of CO_2	PCO2	µatm
Dataset S27	Surface pH	pH	Unitless
Dataset S28	Surface aragonite saturation state	OMar	Unitless

Dataset S29. Horizontal model grid (longitude, latitude)